J. Appl. Comput. Mech., 11(4) (2025) 887-903
DOI: 10.22055/jacm.2024.47896.4822

ISSN: 2383-4536
jacm.scu.ac.ir

Shahid Chamran University of Ahvaz

Journal of Applied and Computational Mechanics

Research Paper

A Systematic Analysis of a Small-Scale HAWT Configuration and Aerodynamic Performance Optimization Through Kriging, Factorial, and RSM Methods

Farzad Ghafoorian[1], Hui Wan[1], Sahel Chegini[2]

[1] Department of Mechanical and Aerospace Engineering, University of Colorado, Colorado Springs, CO 80918, USA, Email: fghafoor@uccs.edu (F.Gh.); hwan@uccs.edu (H.W.)

[2] School of Railway Engineering, Iran University of Science and Technology, Tehran, Iran, Email: sahelchgini@gmail.com

Received September 07 2024; Revised November 28 2024; Accepted for publication November 29 2024.
Corresponding author: F. Ghafoorian (fghafoor@uccs.edu)
© 2024 Published by Shahid Chamran University of Ahvaz

Abstract. The growth of greenhouse gases and the limitations linked to fossil fuels have intensified the drive to exploit renewable energy sources. Wind energy has emerged as an accessible and cost-effective clean energy solution, attracting the attention of scientists. Horizontal axis wind turbines (HAWTs) are widely recognized as a common turbomachine for generating power from wind energy. Nevertheless, enhancing the system's efficiency remains crucial. In this research, a small-scale HAWT is numerically studied using Qblade, a commercial code coupling the blade element momentum (BEM) approach with the actuator disc theory. This study explores the impact of design parameters, including rotor diameter, hub diameter, blade number, blade chord length distribution, twist angle distribution, and airfoil profile, on the turbine power coefficient. Subsequently, optimization efforts are applied to the results obtained for a 3-blade rotor with SG6043 airfoil profile using three distinct optimization methods: Kriging, factorial, and the classical polynomial Response Surface Method (RSM). The proposed geometries generated by the Kriging, factorial, and RSM methods are numerically analyzed using Qblade, yielding maximum C_p values of 0.450, 0.478, and 0.447 respectively. These values represent a respective improvement of 5.6%, 11%, and 5% compared to the base geometry, which had a C_p value of 0.425.

Keywords: Horizontal axis wind turbine; Qblade commercial code; BEM theory; Polynomial response surface; Kriging.

1. Introduction

The surge in greenhouse gas emissions and the consequent global warming, coupled with the escalating costs of fossil fuels, has spurred the imperative for utilizing clean energy sources like solar, wind, and geothermal power [1]. Among these alternatives, wind energy has garnered considerable traction due to its affordability and widespread availability, leading to the emergence of various wind turbine technologies [2]. Wind turbines are categorized through various lenses; one example is their installation location, which divides them into onshore and offshore variants. However, the most essential and widely acknowledged classification of wind turbines hinges on their rotating axis, segregating them into two groups: Horizontal Axis Wind Turbines (HAWTs) and Vertical Axis Wind Turbines (VAWTs) [3]. Although VAWTs present various advantages, including reduced maintenance costs and simpler installation on building rooftops and highways, the predominant type of wind turbines currently deployed remains the HAWT classification [4]. Despite the inherent intricacies in their installation and maintenance, HAWTs favor higher efficiency. HAWTs are known as three-bladed rotors; however, two and four-bladed HAWTs can be occasionally found [5]. HAWTs can also be classified based on rotor diameter. Large turbines with a diameter range of 50-100 meters produce electricity ranging between 1 to 5 MW. Medium turbines have a diameter of 20-50 meters and produce energy in the range of 100 kW to 1 MW. Meanwhile, the small turbines have a diameter of 5-20 meters, yielding output power of 25 to 100 kW [6]. Small-scaled HAWTs can be further categorized into micro, mini, and household types. Micro-scale HAWT rotor diameter ranging from 0.5-1.25 meters, generates energy between 0.004 kW and 0.25 kW. Mini-scale types have 1.25 to 3 meters rotor diameter and produce 0.25 kW to 1.4 kW electricity, and finally, household rotors have 3 to 10 meters rotor diameter and generate electricity from 1.4 kW to 16 kW [7]. In fact, the diameter of the blade rotor is a critical factor in determining the effectiveness of both VAWT and HAWT. It affects turbine performance by altering the swept area and rotor solidity, which in turn influences the formation of eddy flows downstream of the rotor [8]. To predict the aerodynamic performance of turbines, two numerical methods, computational fluid dynamics (CFD) and blade element momentum (BEM), are frequently employed. While the CFD method offers higher accuracy than BEM, it comes at the cost of elevated computational demands and time consumption [9]. It has been suggested that the CFD method is appropriate for the aerodynamic analysis of various single or dual-rotor VAWTs due to their smaller dimensions. However, this method can be

Published online: December 10 2024

costly for larger HAWTs, and it is advisable to employ a periodic solution for one-blade simulation [10]. Ansys Fluent package emerges as a potent commercial tool for CFD modeling, while the Qblade commercial code is considered a robust and expeditious tool for BEM modeling. However, a limitation of Qblade lies in its reliance on a two-dimensional potential solution, rendering it incapable of capturing the wake flow [11]. Parametric studies on HAWTs by the BEM method are commonplace. The number of blades, solidity, rotor diameter, and blade airfoil profile can significantly affect the HAWT performance [12]. The number of blades and the rotor diameter, which directly affect the turbine's solidity, exert a transformative impact on the turbine's aerodynamic behavior. The results showed that the 3-bladed turbine outperforms the 5-bladed counterpart, boasting a higher power coefficient and reduced losses [13]. A HAWT with SG6043 airfoil profile from hub to tip was modeled in Qblade, and by optimizing the chord of blade sections, the maximum power coefficient increased from 0.4 to about 0.5 at TSR = 7.5 [14]. The airfoil profile from the hub to the tip can also be varied. The results of a numerical study showed that the blade composed of two types of NACA2412 and NACA4412 airfoils is more efficient than the blade with a single airfoil type [15]. Another numerical study using Qblade on HAWT with NACA series airfoils including 0020, 0018, 0015, 0012, 5520, 5518, 5515, and 5512 showed that the highest efficiency is obtained from airfoils with NACA55XX, which gives an output power of about 500 kW at a wind speed of 9 m/s [16]. Using both BEM and CFD methods, a study of the optimal angle of attack is conducted on the symmetric NACA 0012 airfoil and the asymmetric NACA 2412 airfoil. It was found that the maximum lift coefficient is increased when the angle of attack increases. Additionally, the asymmetric NACA 2412 airfoil demonstrated enhanced efficiency at TSR = 7 [17] [18]. Setting the pitch angle impact with variations of displacement, namely +6°, +3°, 0°, -3°, -6° to achieve C_p for TSR variations between 3 and 7 using BEM approach, moreover, the pitch angle setting of 0° and +3° has the best effect on turbine performance [19]. Pitch angle influences the angle of attack and flow direction, affecting stall delay and enhancing operational efficiency. The implications of the pitch angle can be observed in both HAWT blade spanwise configurations and the main and auxiliary blades of VAWT [20]. Small-scale HAWT design optimization between different airfoil series and angle of attack between 0 and 20 degrees indicated that the value of lift coefficient and lift-to-drag ratio were optimal for SD7080 airfoil [21]. It should be mentioned that modification of the airfoil profile could enhance turbine performance by postponing stall. Modifying the shape occurs by creating a cavity on the airfoil or modifying the leading or trailing edges to design a bumpy airfoil [22]. Different methods can optimize the investigated parameters. One of the most common and reliable optimization methods is Kriging, which introduces the optimal parameters with the help of the design of experiment (DOE) approach [23]. One method for optimizing VAWTs and HAWTs is Particle Swarm Optimization (PSO), which relies on a surrogate model derived from the Kriging method to predict the optimized C_p under varying operating conditions [24]. Another important te chnique is the Design of Experiments (DOE), which selects design parameters to represent the design space effectively. Given the l imited number of control points, a factorial method is suitable. Various DOE techniques, including Mixture Design, Taguchi Metho ds, and Response Surface Methodology (RSM), serve different purposes: Mixture Design focuses on formulation, Taguchi Methods on process conditions, and RSM addresses both [25]. RSM includes two primary techniques: Central Composite Design (CCD), whic h models and optimizes two to nine independent variables, and Box-Behnken Design (BBD), which models three to seven factors [26]. In fact, RSM integrates mathematical statistics with experimental design, model fitting, regression analysis, and the examinat ion of interactions among independent variables. This approach establishes a mathematical model that can forecast the performa nce of a system's objective function within a defined range based on specified values of the input variables [27]. When comparing Response Surface Methodology (RSM) outcomes with actual data using several statistical metrics, assessing the model's precision, accuracy, and reliability is crucial. Key indicators include Mean Absolute Error (MAE), Mean Squared Error (MSE), Root Mean Squared Error (RMSE), R-squared, and Adjusted R-squared. MAE measures the average absolute deviation from actual values, with lower values indicating better model performance. MSE focuses on squared differences, highlighting larger discrepancies, where lower values reflect greater adequacy. RMSE, the square root of MSE, offers a clearer interpretation of prediction error in the response variable's units. R-squared shows the variance in the dependent variable explained by the model, with higher values indicating better fit. Adjusted R-squared adjusts for sample size and predictors, with higher values suggesting improved model effectiveness [28].

A comprehensive literature review reveals that the conceptual design of wind turbines and their blades significantly impacts their overall performance. This study focuses on a small-scale HAWT selected as a prototype to evaluate the influence of key design parameters on turbine performance, including the C_p values. The numerical analysis was conducted using the open-source software Qblade, which facilitates the simultaneous integration of the Blade Element Momentum (BEM) theory with the driven disk theory for enhanced numerical evaluation. The distinguishing characteristic of Qblade open-source software lies in its ease of accessibility and its capacity to deliver precise results for scientific, engineering, and commercial applications. This software achieves accuracy by integrating two methodologies: the BEM and actuator disc theories. Input parameters utilized within the software include rotor diameter, hub diameter, number of blades, type of blade airfoil profile, chord length distribution, and twist angle distribution across the radial positions of the blade. Subsequently, based on the numerical findings, an optimal three-bladed rotor featuring the SG6043 blade airfoil profile is assessed through three distinct optimization methods. The factorial method, grounded in the Design of Experiments (DOE), along with the classical polynomial response surface method (RSM), is implemented using the original Minitab software. In addition, the kriging optimization method is employed through the Ansys Workbench package. The configurations generated by all three methods are subsequently analyzed numerically using Qblade, and the maximum C_p values are compared with those of the prototype HAWT. As an additional distinguishing characteristic, the maximum C_p results of the proposed configuration, derived from Qblade, are compared with those obtained from the optimization software. This comparison aims to identify the optimization method exhibiting the lowest error percentage. The objective of this study is to conduct a thorough examination of HAWT aerodynamics and to optimize design parameters that have not been extensively investigated previously.

The previous studies employing the Qblade commercial package focused primarily on a general analysis of rotor blade design. In this study, we aimed to address the gaps in previous research by conducting a comprehensive analysis of the HAWT conceptual design parameters. Our objective was to explore the aerodynamic impact of each parameter on rotor efficiency. In addition to a systematic parametric examination, this study introduces an advancement over previous research by specifying three optimization methods. Detailed discussions on these methods and their performance in achieving an optimal design and turbine efficiency optimization are provided. In previous studies, presenting only the results obtained from the Qblade open-source package was sufficient. However, concerns regarding the validity of these results, which are based on the Qblade solution method, have arisen. In this study, we provide a robust validation and compare the results derived from Qblade with existing experimental and numerical findings. We aim to demonstrate the validity of the results based on Qblade application while offering a comprehensive analysis and conceptual design for HAWT. This approach highlights the strengths of our analysis compared to earlier studies and identifies existing gaps in the previous research.

2. Solution Strategy

This section will present a detailed overview of the impending modeling challenges, accompanied by a comprehensive exposition of the governing equations for analysis, efficiency, and rotor conceptual design. Additionally, we will delve into the equations pertaining to the optimization method for the rotor.

2.1. Problem description and methodology

The current research project aims to create and analyze a mathematical model of a small HAWT to enhance its aerodynamic efficiency. This involves utilizing the Qblade commercial code, which integrates the Blade Element Momentum (BEM) method with the actuator disc theory to establish a comprehensive mathematical representation that accounts for the complex aerodynamic behaviors of the turbine blade. The blade is divided into discrete elements, with each section defined by radial position, airfoil profile, chord length, and twist angle. It is important to note that although increasing the number of blade sections and spanwise divisions enhances the accuracy of the simulation, it also results in higher computational costs. The relative wind velocity at each blade section is determined using actuator disk theory or blade element momentum theory. This initial calculation serves as a foundation for establishing the angle of attack while also relying on the assumed lift and drag coefficients for individual blade sections. By leveraging the lift and drag coefficients in conjunction with the geometric data of each section, the tangential and normal force vectors, as well as the resulting thrust and torque of each section, can be ascertained. By summing the contributions from all sections, the total cumulative thrust and torque values for the entire turbine rotor can then be derived. After comprehensively analyzing the aerodynamic forces governing the rotor blade and evaluating turbine efficiency based on power coefficient results, we have utilized various optimization methods such as Kriging, Factorial, and RSM to derive the optimal turbine configuration. By employing each design conceptual parameter as input and assessing the corresponding optimal efficiency, also known as the response surface, we aimed to validate the accuracy and efficacy of these three distinct optimization methods. This approach allows us to assess the precision and efficiency of each technique thoroughly.

2.2. Governing equations for aerodynamic analysis

Lift and drag coefficients are calculated from the following relationships [3]:

$$C_L = \frac{2L}{\rho A V^2} \tag{1}$$

$$C_D = \frac{2D}{\rho A V^2} \tag{2}$$

where L and D are lift and drag forces, respectively. Also, A (m^2) is the blade airfoil profile area cross section, V (m/s) is considered as wind velocity, and ρ is the air density, which is equal to 1.225 (kg/m^3).

BEM iteration variables named axial and radial induction factors are defined as [3]:

$$a = \left(\frac{4\sin^2\phi}{\sigma C_n} + 1\right) \tag{3}$$

$$a' = \left(\frac{4\sin\phi\cos\phi}{\sigma C_t} - 1\right) \tag{4}$$

In the above equations, ϕ is inflow angle, C_t and C_n are tangential and normal force coefficients, respectively, and σ is defined as solidity which depends on the number of blades and chord length. Their mathematical relations are presented below [29]:

$$C_t = C_L \sin\phi - C_d \cos\varphi \tag{5}$$

$$C_n = C_L \cos\phi + C_d \sin\varphi \tag{6}$$

$$\sigma = \frac{cB}{2\pi r} \tag{7}$$

where, B is the number of blades, r is rotor radius, and c is chord length, which varies across each individual section element. The velocity components relative to the rotor plane are illustrated in Fig. 1.

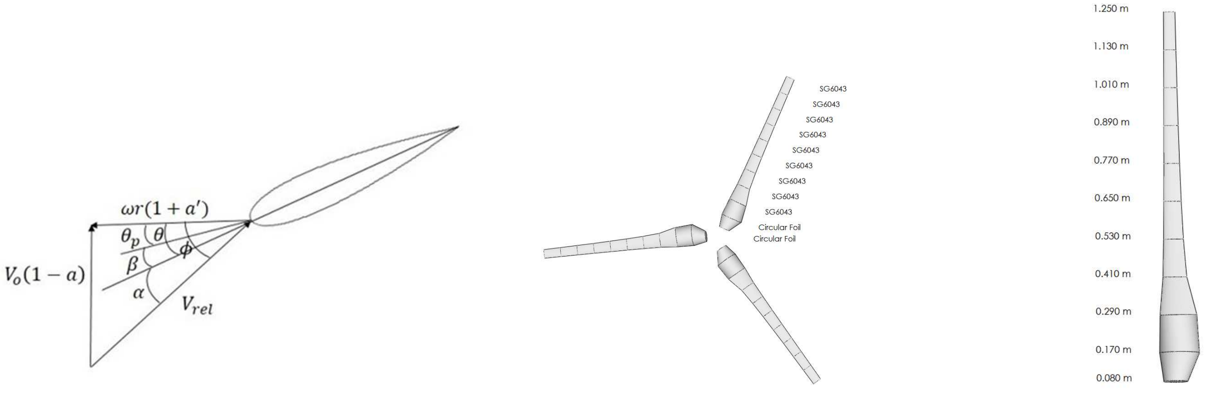

Fig. 1. Velocity vectors at the rotor plane and HAWT schemata.

In Fig. 1, the angle between the relative wind velocity vector (V_{rel}) is defined as the inflow angle (ϕ) and the angle between V_{rel} and the airfoil chord line is defined as the angle of attack (α). Using the induction factors values, the value of the angle of attack is calculated [29]:

$$\alpha = \varphi - \theta \tag{8}$$

$$\theta = \theta_p + \beta \tag{9}$$

In the above equations, θ is the section pitch angle and is the sum of the section twist angle β and the blade pitch angle θ_p. The blade's twist angle (β) is a function of its geometry, while the section pitch angle (θ) changes with blade position and consequently blade pitch angle (θ_p). Note that the angle of attack is the difference between the inflow angle and section pitch angle. In other words, as illustrated in Fig. 1 and expressed in Eqs. (8) and (9), the value of the inflow angle (ϕ) is equivalent to the sum of the angle of attack (α) and the section pitch angle (θ). In this context and throughout the discussion regarding the aerodynamics of the wind turbine, the angle of attack (α) plays a more significant role; thus, Eq. (8) is formulated based on the difference between the inflow angle (ϕ) and section pitch angles (θ). In other words, based on the summation of Eqs. (8) and (9), the angle of attack is not static; it fluctuates in accordance with the geometry of the blade, which encompasses both the twist angle (β) and the blade pitch angle (θ_p). Furthermore, the rotation of the rotor influences blade orientation in relation to the wind direction, thereby affecting the inflow angle (ϕ).

Using the above relationships, new induction factors are obtained by iteration and compared with the previous induction factors. When the maximum value of $(\Delta a, \Delta a')$ is less than the convergence criterion indicated by e value, the calculations are repeated for the next element. The convergence criterion relation is presented below [29]:

$$\max\left(\left|a - a_{old}\right|, \left|a' - a'_{old}\right|\right) \le e \tag{10}$$

The value for e is set to 10^{-5}.

To determine C_p for an ideal rotor design, Eq. (11) is used. However, when taking into account the effects of wake rotation, C_p becomes dependent on the inflow angle. The optimization process for the ideal general rotor includes wake rotation; however, neglects drag ($C_D = 0$) and tip losses ($F = 1$). This optimization assumption is calculated using Eqs. (12) and (13) [11]:

$$C_p = \frac{P}{0.5\rho A V^3} \tag{11}$$

$$C_p = \left(\frac{8}{\lambda^2}\right)\int_{\lambda_h}^{\lambda} \sin^2\phi(\cos\phi - \lambda_r\sin\phi)(\sin\phi + \lambda_r\cos\phi)\left[1 - (C_D / C_L)\cot\phi\right](\lambda_r)^2 d\lambda_r \tag{12}$$

$$\frac{\partial}{\partial\phi}\left[\sin^2\phi(\cos\phi - \lambda_r\sin\phi)(\sin\phi + \lambda_r\cos\phi)\right] = 0 \tag{13}$$

To calculate C_p for the ideal rotor part of Eq. (12) related to the inflow angle, its partial derivative should be equal to zero as shown in Eq. (13). Also, in the above equations, λ is the TSR of a rotor and it depends on rotor rotational speed range and varies according to the specific configuration of the turbine. In simple words, the value of λ changes from the hub to the tip of the turbine blades. While λ_h was the TSR being detected in the rotor hub. λ_r is local TSR, which can be calculated from Eq. (14) and that is different for each spanwise section. The inflow angle is determined from Eq. (15) [11]:

$$\lambda_r = \sin\phi(2\cos\phi - 1) / \left[(1 - \cos\phi)(2\cos\phi + 1)\right] \tag{14}$$

$$\phi = (2/3)\,\mathrm{tg}^{-1}(1/\lambda_r) \tag{15}$$

Axial and Radial induction factors can be calculated by followings [30]:

$$a = 1\big/\left[1 + 4\sin^2\phi / \sigma C_L\cos\phi\right] \tag{16}$$

$$a' = \frac{1 - 3a}{4a - 1} \tag{17}$$

Also, the blade chord length distribution at each section can be calculated with the following relation [11]:

$$c = \frac{8\pi r}{BC_L}(1 - \cos\phi) \tag{18}$$

2.3. Basics of optimization tools

The utilization of the following three methods has been rooted in the purpose of refining the individual input of the target parameters and achieving an optimized response at the optimal point. The two optimization strategies, factorial and Kriging, are aligned with the principles of design of experiments (DOE), and the other is the polynomial response surface method (RSM). DOE methods serve as a fundamental approach to optimization, offering effectiveness in general troubleshooting and the enhancement or refinement of product design and manufacturing processes [31] . In essence, DOE facilitates a systematic and efficient approach for scientists and engineers to explore the correlation between multiple input variables (factors) and essential output variables (responses). It represents a structured methodology for data collection and discovery. DOE is a statistical technique used to optimize the performance of systems with known input variables efficiently. It commences with a screening experimental design test plan encompassing all suspected factors influencing the system's performance (or output). When dealing with a large number of input variables or test factors, the primary objective is to reduce this number to a manageable few. This initial step is typically followed by another experimental design or test plan to optimize the system's performance [32]. The collection of response information involves two primary procedures: firstly, DOE utilizing methods such as factorial and Kriging approach, and secondly, Response Approximation, also known as Surrogate Modeling. Surrogate optimization aims to identify a global minimum of an objective function while minimizing the number of function evaluations. Achieving this entails balancing the optimization process between two objectives: exploration, to identify the global minimum, and speed, to expedite the process [33]. The general DOE procedure can be summarized as following steps [34]:

- Step 1: Consider design variables and response model(s).
- Step 2: Plan the "Design of Experiments (DOE)" across the design space.
- Step 3: Execute experiments or simulations at the designated DOE points.
- Step 4: Develop a response surface spanning the design space.
- Step 5: Establish a confidence interval for the response surface.
- Step 6: Assess model adequacy across the design space.
- Step 7: If the model is deemed inadequate, return to step 1 to refine the model.

2.4. Governing equations for rotor optimization

In the Kriging optimization approach, it is assumed that to predict a function at a specific point, an uncertainty associated with this estimate is considered. Assuming the continuity of the function, two points x_i and x_j are defined and it is expected that the values of $y(x_i)$ and $y(x_j)$ will be closer when reducing the distance $\|x_i - x_j\|$. If the result of this subtraction is small, the random variables $y(x_i)$ and $y(x_j)$ will have an acceptable correlation. This correlation is defined as follows [35]:

$$corr\left[y(x_i, y(x_j)\right] = \exp\left(-\sum_{l=1}^{d}\theta_l \left|x_{il} - x_{jl}\right|^{p_l}\right) \tag{19}$$

The hyperparameter θ_l indicates the speed rate of correlation as moving along the l coordinate direction. Also, p_l determines the function smoothness.

The uncertainty associated with the function values for n points can be defined by the random vector Y. This vector and its covariance matrix are represented by the following mathematical relations [35]:

$$Y = \begin{pmatrix} Y(x_1) \\ \vdots \\ Y(x_n) \end{pmatrix} \tag{20}$$

$$\text{cov}(Y, Y) = \sigma^2 \psi \tag{21}$$

where σ^2 is variance and ψ is $n \times n$ correlation matrix defined as [36]:

$$\psi = \begin{pmatrix} corr\left[Y(x_1), Y(x_1)\right] & \cdots & corr\left[Y(x_1), Y(x_n)\right] \\ \vdots & \ddots & \vdots \\ corr\left[Y(x_n), Y(x_1)\right] & \cdots & corr\left[Y(x_n), Y(x_n)\right] \end{pmatrix} \tag{22}$$

The final kriging prediction from the input data is defined as follows [36]:

$$\bar{y}(x^*) = \bar{\mu} + \Psi^T \psi^{-1}(y - 1\bar{\mu}) \tag{23}$$

where,

$$\bar{\mu} = \frac{1^T \psi^{-1} y}{1^T \psi^{-1} 1} \tag{24}$$

$$\Psi = \begin{pmatrix} corr\left[Y(x^*), Y(x_1)\right] \\ \vdots \\ corr\left[Y(x^*), Y(x_n)\right] \end{pmatrix} = \begin{pmatrix} \Psi_1 \\ \vdots \\ \Psi_n \end{pmatrix} \tag{25}$$

For the factorial method based on the design of experiments (DOE), the design space is evenly populated with points, and each factor is divided into n levels. The number of runs required for optimization is calculated using the factorial method from the following equation [37]:

$$Run = L^f \tag{26}$$

In the current study, there are 5 factors, each divided into four levels. As a result, the number of runs needed to optimize and present the experiment design will be equal to 4^5.

The response surface methodology (RSM) is chosen for the simulation of problems in which the response of interest is affected by multiple independent variables, with the aim of optimizing this response. In this context, the primary objective is to establish an approximation for the relation between variables and the response. This relationship can be described by a linear function, or, if it contains curvature in the system, by higher-order polynomial functions. For the optimization process conducted in the current study, a second-order polynomial was selected, as shown in the following relation [37]:

$$y = \beta_0 + \sum_{i=1}^{k}\beta_i x_i + \sum_{i=1}^{k}\beta_{ii} x_{ii}^2 + \sum_{i=1}^{k}\sum_{j=i+1}^{k}\beta_{ii} x_i x_j + \varepsilon \tag{27}$$

where y represents the response of interest, x_i and x_j denote the independent variables, β_i, β_{ii} and β_{ij} are the coefficients to be determined, k is the number of independent variables, and ε is the experimental error associated with the approximation.

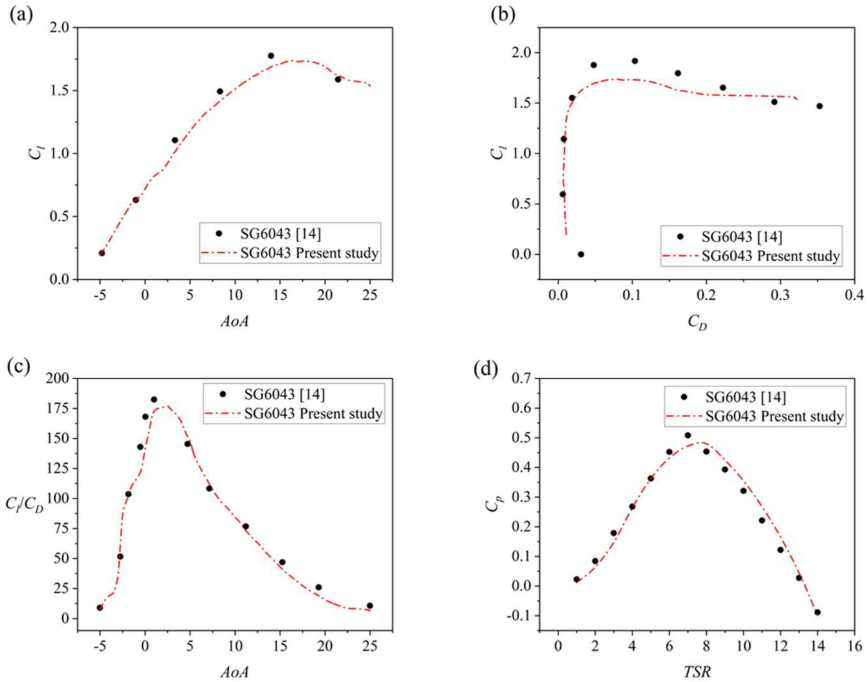

Fig. 2. (a) Lift and drag coefficients as a function of angle of attack, (b) Lift coefficient as a function of drag coefficient, (c) Lift to drag coefficient as a function of angle of attack, (d) C_P value for HAWT for different TSR values.

3. Model Validation

In order to verify the validity of the current numerical modeling, a study by Alaskari et al. [14], on a HAWT with the S-series airfoil profile (SG6043) with the same dimensions for rotor as the current study was selected. The data from the reference, and the results of the present analysis, both based on Xfoil direct analysis data, are presented in Fig. 2.

In Fig. 2, the lift coefficient at different AoA values is significantly high enough, which shows the efficacy of SG6043 for HAWT design in the low Reynolds number range of 5×10^5. Notably, the highest lift coefficient value reaches 1.8 at 14° AoA. Furthermore, the peak C_L/C_D value reaches 177 at an AoA of 2.5°. Regarding the validation, it is discernible that the outcomes obtained through the Qblade commercial code exhibit a commendable concordance with the results of Alaskari et al. [14]. From Fig. 2(a), the highest error percentage for the lift coefficient occurred at an AoA of 14°, which is equivalent to 5.6%. Similarly, for Fig. 2(b) and 2(c), the highest error percentage was equal to 9.7% and 7.2%, respectively. Additionally, Fig. 2(d) compares the overall power coefficient of the HAWT based on Alaskari et al. [14] and numerical results. Notably, the numerical outputs obtained from Qblade exhibited an acceptable level of agreement with the results of the reference article. It is essential to highlight that the most significant deviation between the two outputs transpired at TSR = 8, with a value of 6.4%. Consequently, taking into consideration the error magnitudes and the coherent trend of the graphs in the recent study alongside those from the reference study, the validity of the results is acceptable. Consequently, the validity of the results is acceptable, considering the error magnitudes and coherent trend of the graphs in the recent study alongside those from the reference study. The results obtained from the QBlade commercial package are derived from XFoil data, which suggests that these findings can be regarded as reliable. Furthermore, additional validation will be presented at the end of the simulation process to illustrate the robustness and effectiveness of the current parametric study and optimization based on experimental data from another small-scale HAWT.

Table 1. Dimensions and main geometric specifications of the simulated HAWT.

Quantity	Value
Number of blades (B)	3
Rotor diameter (D)	2.5 (m)
Hub diameter (d)	0.16 (m)
Blade airfoil profile	NACA4412

Table 2. Blade design parameters.

Section number	Radial position (m)	Chord length (m)	Twist angle (degree)
1	0	0.076	0
2	0.09	0.126	0
3	0.21	0.119	18.312
4	0.33	0.076	12.191
5	0.45	0.063	8.660
6	0.57	0.055	6.379
7	0.69	0.050	4.789
8	0.81	0.045	3.619
9	0.93	0.042	2.722
10	1.05	0.039	2.014
11	1.17	0.036	1.440

4. Rotor Design and Numerical Settings

The Qblade design tool has been used for the purpose of formulating the geometry of the examined HAWT. The rotor blades are divided into eleven discrete sections. The first two sections characterize a circular cross-section. The remaining blade sections, spanning from the hub to the tip, adhere to the same blade airfoil profile. Geometric specifications are presented in Table 1. Also, pertinent details concerning the distribution of twist angles and blade chord lengths have been listed in Table 2.

NACA4412 airfoil profile is categorized as low Reynolds number airfoils. Based on the Xfoil data suggestions for the NACA4412 airfoil profile, in this simulation, Reynolds number 5×10^5 and Ncrit number 9 are considered. Also, the considered angle of attack ranges from -5° to 25°. These values for Reynolds and Ncrit numbers signify turbulent flow within the realm of a low Reynolds number range. The selected values reflect the conditions representative of an average wind tunnel environment, neither exceptionally clean nor heavily laden with contaminants.

5. Results and Discussion

In this section, we present a comprehensive analysis of the parametric study conducted on the aforementioned HAWT. Our investigation focuses on examining the influence of various parameters, including rotor diameter, hub diameter, number of rotor blades, twist angle distribution, chord length distribution, and blade airfoil profile, on both the aerodynamic performance and overall system efficiency. Only the target parameter is varied in each step of the parametric study, while the other design parameters remain constant, according to Tables 1 and 2. It is important to acknowledge that the evaluation of design parameters considered as inputs is based on the prior research conducted by Alaskari et al [14]. This study categorized the design parameters, dimensions, and specifications within the small-scale HAWTs group, along with all corresponding blade airfoil profiles, which have been effectively implemented and operated for small-scale HAWTs blade spanwise. Furthermore, any modifications to the design parameters range at each stage have been carefully executed to ensure that these turbine variations remain within the small-scale classification. Additionally, careful consideration has been given to ensure that the results of the parameter study for all ranges of design parameter modifications do not exceed the Betz limit for C_p output. The Betz limit for HAWTs is established at a maximum of 0.55 [3]. Consequently, throughout the simulation and adjustment of design parameters, the range of parameter changes is meticulously maintained to prevent any overestimation of the Betz limit. This limit serves as a critical benchmark that assures the validity of the mathematical simulations for HAWTs.

5.1. Effect of rotor diameter

Four distinct values, specifically 1.4 (m), 2.5 (m), 3.6 (m), and 4.66 (m), have been considered for the rotor diameter of the three-bladed turbine. The selection of the parameter was made with the objective of evaluating diameters that are both smaller than the base configuration condition, as well as those that are larger in size. This measure was implemented to ensure that the full spectrum of diametric values were tested and accounted for in the analysis. The results of turbine power coefficient (C_p) in relation to Tip Speed Ratio (TSR) are presented in Fig. 3.

The findings presented in Fig. 3 demonstrate that turbines with larger rotor diameters have a wider operational range, resulting in the ability to generate power across a broader range of TSR values. Conversely, turbines with smaller diameters encounter operational challenges in the high TSR range. Nonetheless, their increased solidity results in improved efficiency at low TSRs and reduced initial torque required for initiation. Upon closer examination of turbines with diameters of 1.4 (m), 2.5 (m), 3.6 (m), and 4.66 (m), the peak C_p values of 0.42, 0.43, 0.46, and 0.4 at TSRs of 5, 8, 11, and 14, respectively, reveal that the rotor with a diameter of 3.6 m achieved the highest power coefficient among the investigated cases. It is worth noting that the observed reduction in the efficiency of the rotor with a diameter of 4.66 can be mainly attributed to the physics of the flow. Specifically, the utilization of the low Reynolds number airfoil profile NACA4412 does not result in the necessary efficiency for HAWTs with large diameters. Consequently, alternative airfoil profiles may require consideration to optimize the performance of HAWTs in such scenarios.

5.2. Effect of hub diameter

In this section, we investigate the impact of hub diameter by examining four distinct values: 0.08 (m), 0.12 (m), 0.16 (m), and 0.2 (m). Figure 4 illustrates the results of the influence of hub diameter on the turbine's C_p relative to TSR.

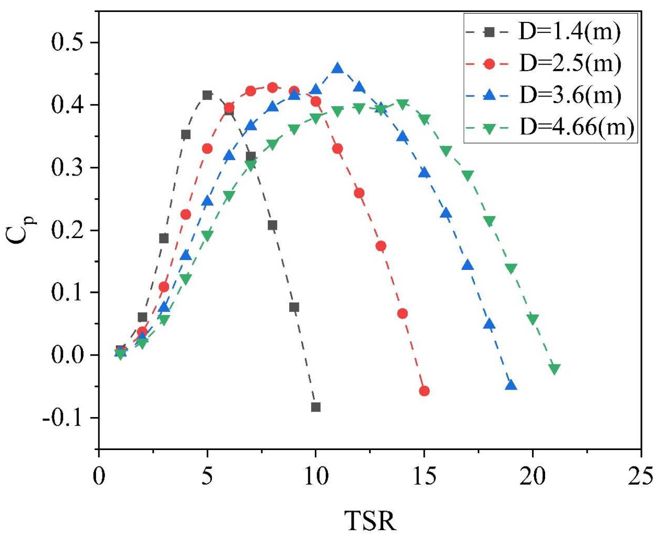

Fig. 3. C_p values for different rotor diameters.

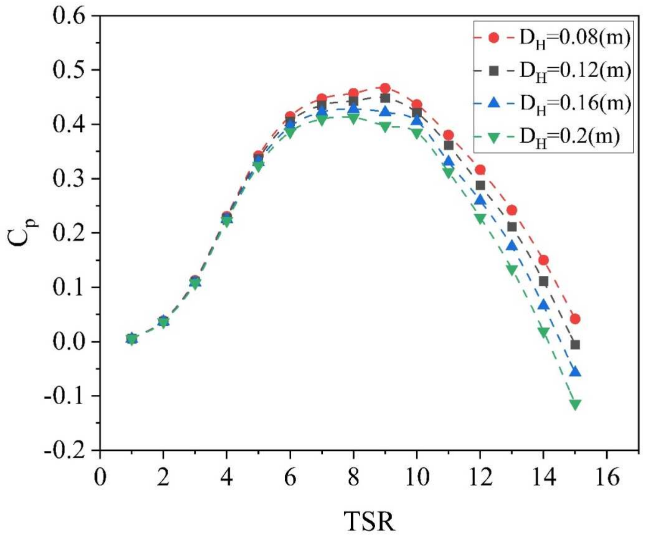

Fig. 4. C_p values for different hub diameters.

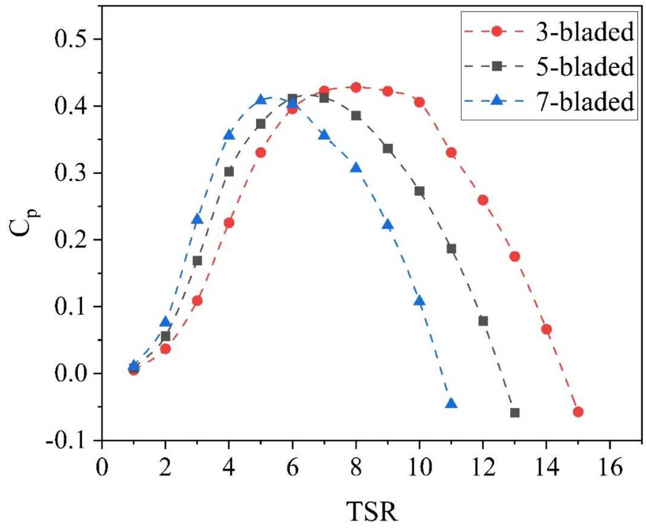

Fig. 5. C_p values for different numbers of blades.

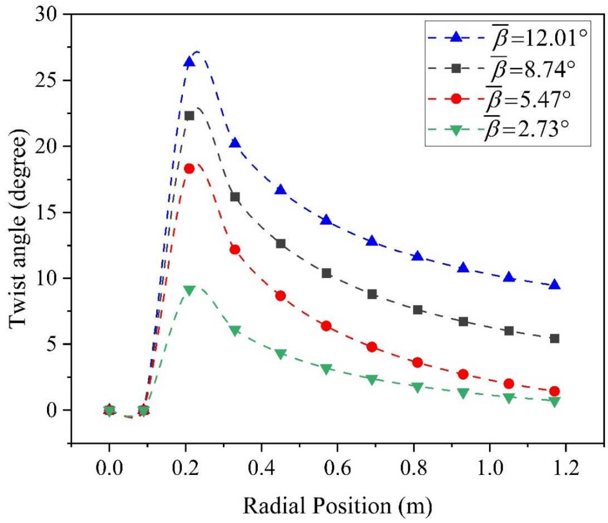

Fig. 6. Twist angle distribution along the blade.

According to Fig. 4, hub diameter alterations did not significantly affect the range of TSRs. In addition, an increase in hub diameter led to a decrease in C_p values. A more detailed analysis revealed that peak C_p values of 0.47 and 0.45 were attained at the TSR of 9 for hub diameters of 0.08 m and 0.12 (m), respectively. Conversely, maximum C_p values of 0.43 and 0.41 were achieved at TSR 8 for hub diameters of 0.16 (m) and 0.2 (m), respectively. The limited impact of the hub diameter on rotor efficiency is attributable to the absence of significant changes in the flow physics and aerodynamics of the rotor. Specifically, changes to the diameter of the hub only impact the location of the blades, thereby having minimal effects on the flow regime. Consequently, changes in operating range and C_p are imperceptible.

5.3. Effect of number of blades

In this section, we examine the effect of the number of blades on the prototype, which directly affects the rotor's solidity. Two models are considered: one with five blades and another with seven blades. The impact of the number of blades on C_p relative to TSR is presented in Fig. 5.

Upon examining Fig. 5, it becomes evident that the 3-bladed HAWT rotor has a broader operational TSR range. However, the 7-bladed rotor, characterized by a higher solidity than the other configurations, exhibited higher initial TSR values for its C_p. This underscores its ability to initiate rotation with lower initial torque. Furthermore, it is observed that rotors with three, five, and seven blades achieved peak C_p values of 0.43, 0.41, and 0.4, respectively, at TSR values of 8, 7, and 6. These intricate observations substantiate the fact that the 3-blade HAWT rotor showcased superior efficiency compared to other configurations, albeit by a slight margin. It is noteworthy that the number of blades has an analogous effect on the output power of the turbine, as observed in C_p. An increase in blade count restricts the operational range of the turbine. The proliferation of blades within a HAWT has resulted in a corresponding increase in the solidity of the rotor, which has led to blade-to-blade interaction. This phenomenon is detrimental to the aerodynamic performance of the HAWT and has resulted in a limited range of TSR. In light of this, it is crucial to address the issue of blade-to-blade interaction to improve the operational efficiency of the HAWT. Also, from solid mechanics point of view, it can be argued that the addition of blades to a rotor not only enhances its solidity but also causes a displacement in its center of mass, which could lead to moments that potentially reduce the efficiency and operational range of turbines with more blades [3, 30].

5.4. Effect of Twist angle distribution

In this section, we study the effect of twist angle distribution along the turbine blade. Four distinct twist angle distributions are considered for a blade, which is divided into eleven sections as aforementioned. The specific twist angle values and their corresponding radial positions are documented in Table 3. Moreover, Fig. 6 illustrates the twist angle distribution along the radial positions.

Referring to the data presented in Table 3, it is evident that the two circular sections adjacent to the hub consistently maintain a twist angle of 0° across all examined cases. Notably, the calculated average twist angle values for cases 1, 2, 3, and 4 are 2.73°, 5.47°, 8.74°, and 12.01°, respectively. Furthermore, as depicted in Fig. 6, the distribution of twist angles along the radial position of the blade, spanning from the hub to the tip, exhibits a similar trend across all cases. The twist angle experiences a pronounced transition in proximity to the hub, followed by a gradual and consistent reduction towards the blade's tip.

Table 3. Twist angle distribution.

Radial position (m)	$\bar{\beta}$ = 2.73°	$\bar{\beta}$ = 5.47°	$\bar{\beta}$ = 8.74°	$\bar{\beta}$ = 12.01°
0	0	0	0	0
0.09	0	0	0	0
0.21	9.16	18.32	22.32	26.32
0.33	6.095	12.19	16.19	20.19
0.45	4.33	8.66	12.66	16.66
0.57	3.19	6.38	10.38	14.38
0.69	2.395	4.79	8.79	12.79
0.81	1.81	3.62	7.62	11.62
0.93	1.36	2.72	6.72	10.72
1.05	1.005	2.01	6.01	10.01
1.17	0.72	1.44	5.44	9.44

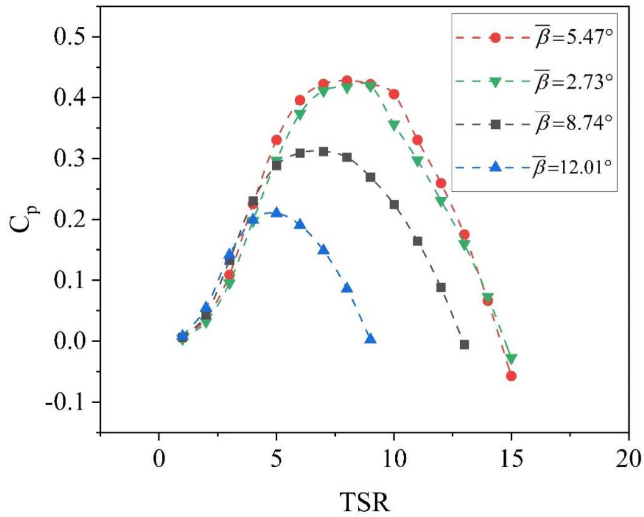

Fig. 7. C_p values for different twist angle distributions.

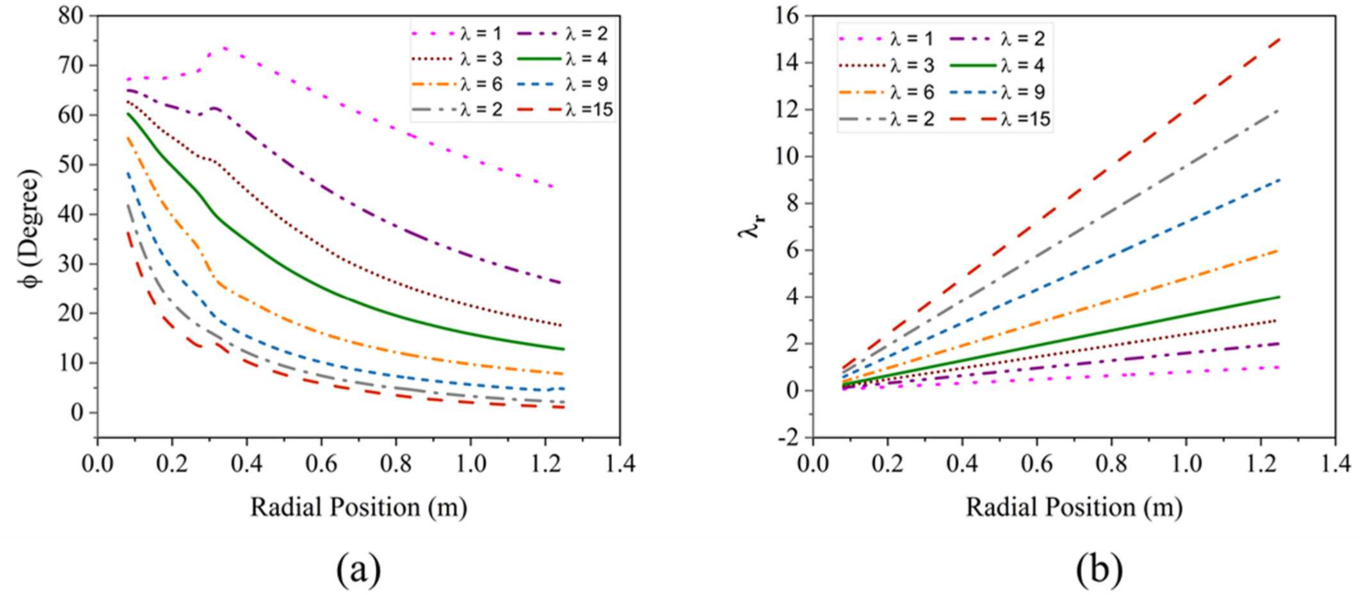

Fig. 8. Rotor characteristic curve for $\bar{\beta}$ = 5.47° configuration, (a) Inflow angle, (b) Local TSR.

Figure 7 illustrates the effect of different twist angle distributions on HAWT performance. The presented data in Fig. 7 reveals that extending the twist angle distribution along a turbine's radial position substantially influences its TSR range. It is noteworthy, however, that an excessive amplification in the twist angle distribution can result in reduced efficiency. In particular, the rotor with an average twist angle distribution of 2.73°, 5.47°, 8.74°, and 12.01° exhibits the peak C_p values of 0.42, 0.43, 0.31, and 0.21 at respective TSR values of 9, 8, 7, and 5. The modification of the twist angle of a turbine has significant implications for its inflow angle and angle of attack, which, in turn, influence both the tangential and normal forces percolating through each rotor section. The results of this change reveal that turbines equipped with a higher twist angle are characterized by a reduced lift force in each spanwise section, thereby restricting their efficiency and operating range.

The following discussion in Fig. 8 presents two cases of HAWT characteristic curves. The first case illustrates the inflow angle in terms of radial position, while the second case demonstrates the local tip speed ratio in terms of radial position.

The effectiveness of a wind turbine is contingent on the inflow angle and local TSR. Among the various configurations, the rotor configuration with $\bar{\beta}$ = 5.47° offers the utmost efficiency. Each curve denotes a TSR or angular velocity in the HAWT characteristic curve. This particular configuration operates within the TSR 1 to 15 range, and each characteristic curve represents 15 curves; however, in order to prevent any data confusion, only 8 curves have been presented. According to Fig. 8(a), as the TSR increases, the inflow angle declines. Additionally, the inflow angle displays a decreasing trend from the hub to the tip along the radial position. Notably, the radial position of TSRs 1 and 15 exhibits the highest and lowest inflow angle values ranging from 68° to 45° and 38° to 5°, respectively. It is pertinent to mention that the rate of change for inflow angle is more pronounced in smaller TSRs. It is essential to recognize that, following Eqs. (8) and (9) and the velocity triangle depicted in Fig. 1, the inflow angle corresponds to the angle of attack based on the rotor's rotation and the orientation of the velocity vector concerning the blade and the section pitch angle. The section pitch angle itself is influenced by the blade pitch angle and the twist angle at each radial position and that is a geometrical parameter. Consequently, fluctuations in the inflow angle and subsequently angle of attack which is dependent on inflow angle, blade pitch angle and twist angle, particularly in relation to the twist angle across various radial positions, are predictable. In other words, both the inflow angle and the angle of attack are influenced by the rotor position and the orientation of the blades. These factors are associated with the TSR or angular velocity, rotor rotation, and blade geometry, which correspond to the radial position along the blade length.

Table 4. Chord length distribution.

Radial position(m)	$\bar{C}$ = 0.066 (m)	$\bar{C}$ = 0.089 (m)	$\bar{C}$ = 0.111 (m)	$\bar{C}$ = 0.159 (m)
0	0.076	0.076	0.076	0.076
0.09	0.126	0.151	0.176	0.226
0.21	0.119	0.144	0.169	0.219
0.33	0.076	12.19	0.126	0.176
0.45	0.063	0.101	0.113	0.163
0.57	0.055	0.088	0.105	0.155
0.69	0.05	0.08	0.1	0.15
0.81	0.045	0.075	0.095	0.145
0.93	0.042	0.07	0.092	0.142
1.05	0.039	0.064	0.089	0.139
1.17	0.036	0.061	0.086	0.136

The analysis of Fig. 8(b) indicates that a rise in TSR leads to a corresponding increase in the local TSR along the radial position from the hub to the tip. Specifically, at $\lambda = 1$, the local TSR ranged from 0.6 to 1. Subsequently, with a rise in rotational speed at $\lambda = 15$, the local TSR range achieved the range of 1.6 and 15, and witnessed a significant increase. It is also evident from the characteristic curve of the rotor that the local TSR value at the tip of the blade at the position of 1.25 meters was exactly equal to the TSR of the turbine.

5.5. Effect of chord length distribution

In this section, we investigate the effect of chord length distribution along the radial position. The number of blade sections remains constant at eleven, and the other design parameters are unaltered. Four various chord length distributions are examined for current HAWT. Each section's radial position and the corresponding chord length are listed in Table 4. Furthermore, Fig. 9 illustrates the chord length distribution along the turbine blade.

The analysis of Table 4 reveals that the chord length value at the first circular section connected to the turbine hub is consistent across all four cases. The mean chord length values for cases 1 to 4 are 0.066 (m), 0.089 (m), 0.111 (m), and 0.159 (m), respectively. Figure 9 demonstrates that the chord length at the second circular section increases remarkably. However, after a sharp decline, the chord length at subsequent sections decreases steadily until the turbine tip. The solidity of the rotor blade, which is directly related to the blade chord length, is significantly enhanced by increasing the chord length distribution along the radial position, resulting in a high-solidity turbine. It is evident that, for each design, the rotor solidity near the blade hub is greater than that at the blade tip. Furthermore, Fig. 10 provides evidence of the impact of different chord length distributions on the HAWT performance.

The findings associated with Fig. 10 suggest that the blade chord length distribution has a discernible impact on the rotor operating range. Specifically, a higher chord length distribution values along a radial position of 0.159 (m) in the high-solidity rotor resulted in a reduced TSR operating range. Further, high-solidity turbines exhibited higher C_p values at lower TSRs compared to others, indicates that turbines with a more significant chord length distribution can generate greater torque value and experience an increased static torque coefficient within a low TSR range. These turbines, due to their enhanced chord length distribution, require less initial torque to initiate operation. HAWTs, which typically operate based on lift force, face challenges with self-starting capabilities and thus necessitate initial torque to commence functioning. Therefore, a higher chord length distribution facilitates an increased torque value, effectively addressing the issues associated with self-starting and the generation of initial torque. A closer analysis reveals that turbines featuring average chord length distributions of 0.066 m, 0.089 m, 0.111 m, and 0.159 m achieved peak C_p values of 0.43, 0.48, 0.49, and 0.48, respectively, corresponding to TSRs of 8, 6, 5, and 4. It is worth noting that the turbine with an average chord length distribution of 0.111 m achieved the maximum C_p value. As expected, the maximum value of C_p was obtained for more solidity rotors in smaller TSR ranges.

5.6. Effect of blade airfoil profile

In this section, we study the effect of blade airfoil profile on HAWT performance. To achieve this objective, two distinct categories of airfoils are investigated, the NACA series and the S-series, both as low Reynolds number airfoils. NACA0018 and NACA0021 airfoil profiles are symmetrical, and other airfoil profiles are asymmetrical. The geometric characteristics of airfoils are documented in Table 5 [38].

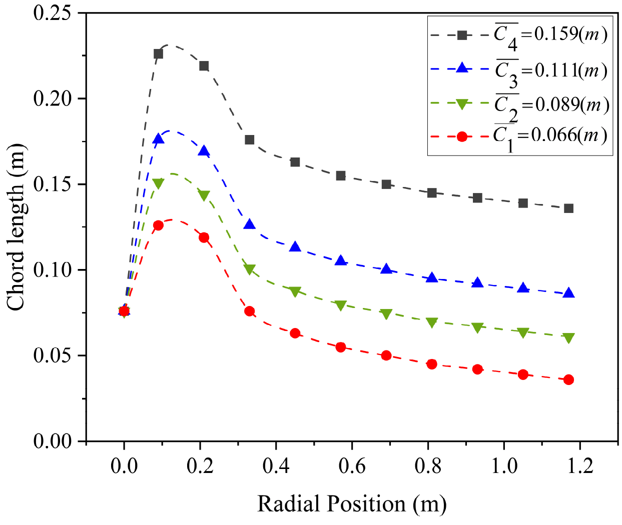

Fig. 9. Chord length distribution along the blade.

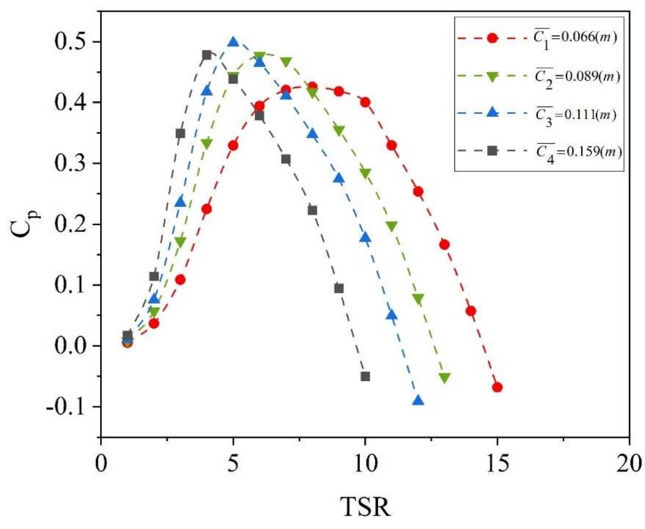

Fig. 10. C_p values for different chord length distributions.

Table 5. Geometric characteristics of airfoils.

Airfoil profile	Thickness (%)	Camber (%)
NACA0021	21.00	0
NACA0018	18.00	0
NACA2412	12.00	2.0
NACA4412	12.00	4.0
SG6050	16.01	3.24
SG6043	10.02	5.50
SG6040	16.00	2.50
SP6421	21.07	4.02

It can be seen from Table 5 that NACA4412 has the highest camber and NACA0021 has the highest thickness among NACA series airfoils, while SG6043 has the highest camber and SP6421 had the highest thickness in S-series airfoil profiles. The Reynolds number and Ncrit number are set to 5×10^5 and 9, respectively. Also, the angle of attack considered is between -5° to 25°. Analysis of aerodynamic forces obtained from Xfoil direct analysis data is given in Fig. 11.

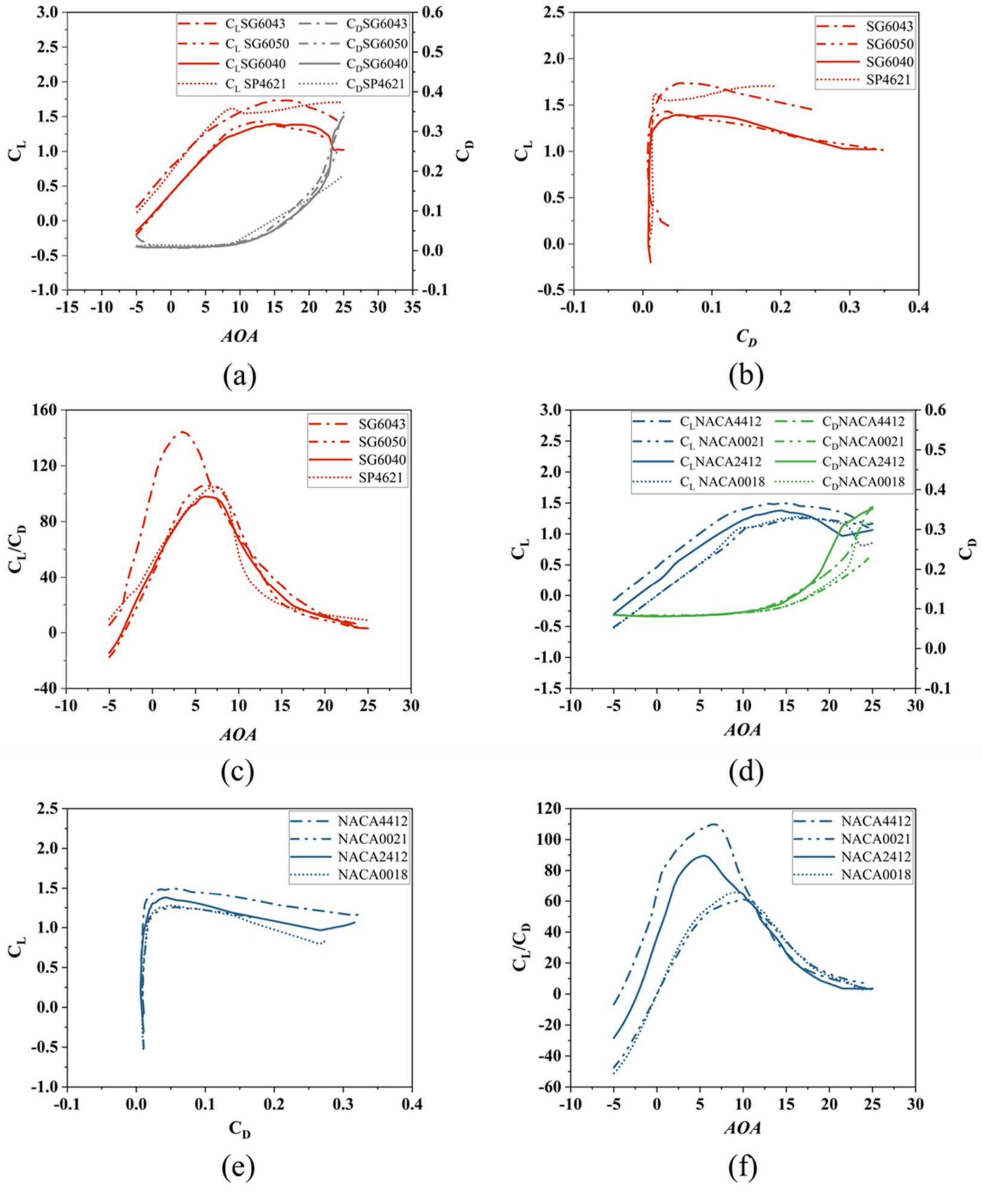

Fig. 11. (a) Lift and drag coefficients as a function of angle of attack for S-series airfoil profiles, (b) Lift coefficient as a function of drag coefficient for S-series airfoil profiles, (c) Lift to drag coefficient as a function of angle of attack for S-series airfoil profiles, (d) Lift and drag coefficients as a function of angle of attack for NACA series airfoil profiles, (e) Lift coefficient as a function of drag coefficient for NACA series airfoil profiles, (f) Lift to drag coefficient as a function of angle of attack for NACA series airfoil profiles.

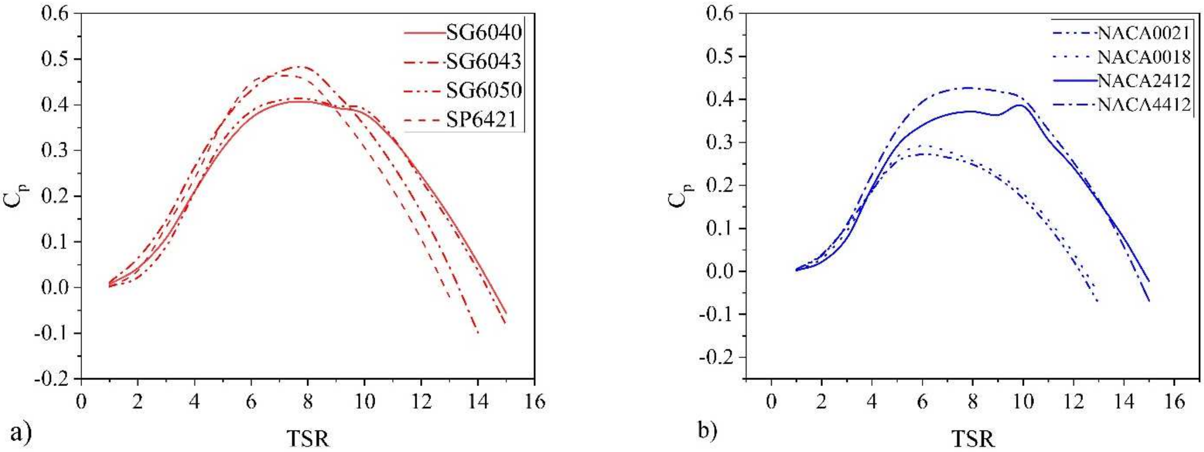

Fig. 12. (a) C_p values for blades with S-series airfoil profile, (b) C_p values for blades with NACA series airfoil profile.

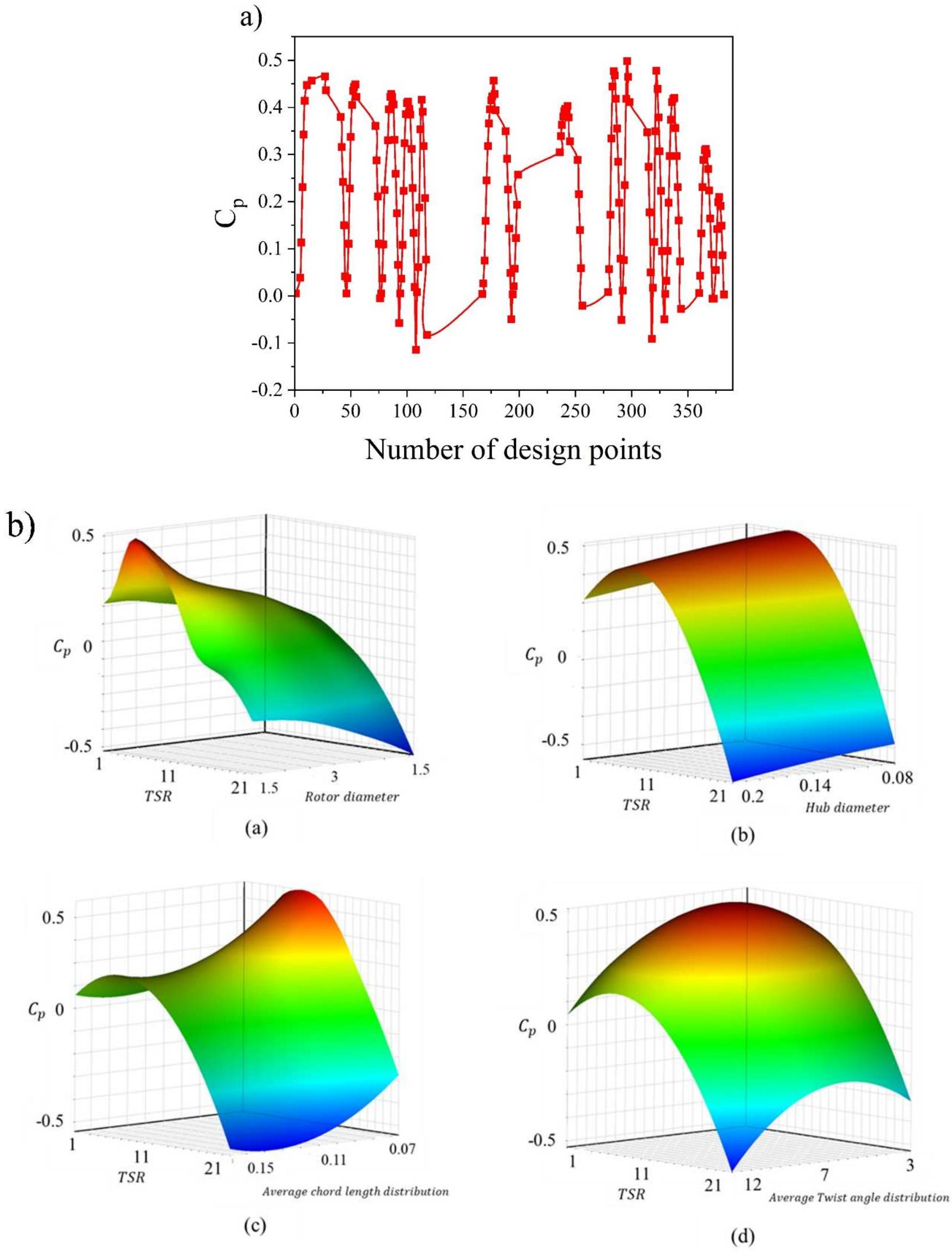

Fig. 13. (a) Number of input design points, **(b)** RSM results of Maximum C_p for changes in, (a) rotor diameter, (b) hub diameter, (c) chord length distribution, (d) twist angle distribution.

Table 6. Optimized configuration.

Optimization method	Rotor diameter (m)	Hub diameter (m)	Average chord length distribution (m)	Average twist angle distribution (degree)
Kriging	4.12	0.08	0.066	5.47
Factorial	4.66	0.08	0.066	2.73
RSM	4.03	0.08	0.066	5.47

Table 7. Optimal C_p for different optimization methods.

Case	Maximum C_p with analytical application	Maximum C_p with Qblade	Error (%)
Kriging	0.473	0.450	5.1
Factorial	0.441	0.478	7.7
RSM	0.433	0.447	3.1
Base case	-	0.425	

From Figs. 11(a) and 11(d), the obtained lift coefficients are significantly higher than the drag coefficients, which means that all S and NACA series airfoils are suitable for designing turbomachines that operate primarily based on the lift force. In addition, the highest C_L values for all airfoils, ranging from 1.3 to 1.6, are consistently achieved at an AOA of 15°. Also, based on Fig. 11 and the values of the lift coefficients, it is clear that among the S-series airfoils, those with more pronounced camber, specifically SP6421 and SG6043, achieve higher C_L values compared to their counterparts. Asymmetric airfoils from the NACA series also exhibit higher lift coefficients than symmetric counterparts within the AOA range of -5° to 10°; however, at higher AOA values, the NACA0021 exhibit higher C_L than other investigated NACA airfoils. Additionally, Fig. 11(c) reveals that the essential parameter lift-to-drag ratio for SG6043 reaches 150 at AOA of 4°, notably higher than the maximum of C_L/C_D achieved by other S- series airfoils, which typically ranges between 80 and 100 at a larger AOA of approximately 8°. In Fig. 11(f), the maximum value of C_L/C_D for NACA4412 is obtained at an AOA of 7°, surpassing other profiles. Meanwhile, the NACA2412 airfoil achieves a maximum C_L/C_D value of 90 at 5° AOA. Symmetric airfoils exhibit a maximum C_L/C_D of 64 at 8° AOA. The impacts of these various airfoil profiles on turbine performance are illustrated in Fig. 12.

From Fig. 12 a, it can be seen that the operating range of the HAWT rotor with the blades consisting of the SG6050 and SG6040 airfoil profiles boasts a slightly broader operational range compared to those utilizing SG6043 and SP6421 airfoils. Interestingly, the inclusion of the latter two airfoils, characterized by substantial camber values and lift coefficients, results in an enhanced maximum power coefficient. Specifically, the maximum power coefficients for SG6050, SG6043, SG6040, and SP6421 airfoils amount to 0.42, 0.48, 0.41, and 0.46, respectively. With the exception of the SP6421 profile, which attains its maximum C_p value at TSR = 7, the others achieve peak C_p values at TSR = 8. According to Fig. 12(b), the operating range and maximum efficiency of the HAWT turbine with blades designed with asymmetric airfoils are higher than the blade consisting of symmetrical airfoils. For the blade with NACA0018, NACA0021, NACA2412, and NACA4412 airfoils, the maximum C_p values are 0.29 and 0.28 at TSR = 6, and 0.37 and 0.43 at TSR = 8, respectively. As illustrated in the Fig. 12, the range of achievable C_p across configurations utilizing NACA series and S-series airfoils is highlighted by the blades designed with SG6043 and NACA0021 airfoils, representing the highest and lowest values, respectively.

5.7. Rotor optimization

In this section, we study the optimized configuration for studied HAWT. To achieve this aim, the blade airfoil SG6043 with 5.5% camber is considered, and the 3-bladed rotor is selected for the optimum configuration. Various design parameters, including rotor diameter, hub diameter, chord length, and twist angle distribution along blades, will undergo optimization. To achieve this, three different optimization approaches are being employed: the Kriging optimization method, the factorial method based on the Design of Experiments (DOE) approach, and the classical polynomial response surface method (RSM). The design parameters mentioned above, as well as the TSR, serve as input parameters, while the power coefficient functions as the objective function or the response surface. The philosophy underpinning DOE-based optimization methods revolves around the individual definition of parameters as design parameters for the optimization function. Subsequently, the effect of each parameter is systematically evaluated on the response surface as the output object. The design point parameter obtained vs C_p upon solving as response surface or output parameter are shown in Fig. 13(a). The Kriging optimization process is conducted in the Ansys Workbench package. For the factorial method and RSM, the Minitab application is selected. The response surface diagrams and the optimized parameter values are presented in Fig. 13b and Table 6, respectively.

In Fig. 13(a), the 5 design parameters specified as inputs for the optimization function have resulted in 380 design points, displayed on the horizontal axis as inputs for the DOE optimization method. The upper and lower limits of C_p are represented as the output response for each of the 382 design points on the vertical axis. In other words, in accordance with the optimization methods derived from the DOE approach, the input parameters along with various modes were juxtaposed based on the results obtained from these methodologies and the corresponding number of test cases as sample points. This study evaluates four design parameters: rotor diameter, hub diameter, averaged twist angle, and averaged chord length, in conjunction with TSR as an operational parameter for DOE inputs, reflecting the value of C_p for the output or response point obtained in each sample case. Consequently, a total of 382 sample points were designed for the analysis. The upper limit of C_p, determined through analysis using Qblade and equal to 0.48, demonstrates acceptable agreement with DOE output upper limit; therefore, it can be stated that the optimization approach is valid. Based on the information in Fig. 13(b) and Table 6, it can be seen that optimizing the design parameters of the rotor is not solely contingent to maximize C_p at a specific TSR. The rotor's operational range also plays a significant role in influencing the optimization results. More precisely, while $\bar{C}$ = 0.159 (m) achieved the highest C_p due to its superior chord length distribution along the blade, $\bar{C}$ = 0.066 (m) was selected as the optimal choice because this case had a broader operational range and the fact that its C_p values declined more gradually compared to other cases. Each of the optimization methods has different precision due to its mathematical formulation and the partitioning of parameters at different levels. Consequently, discrepancies arise in achieving optimal results for certain parameters. Therefore, the obtained optimum results are subject to validation. They are re-evaluated using Qblade and compared with the base case results. Table 7 shows the results for the maximum C_p obtained from each optimization method, compared to the maximum C_p obtained from the reanalysis of the optimal configuration using Qblade and the base case. In other words, the value of C_p obtained utilizing the optimal values for the turbine's conceptual design parameters, as determined by different methods (presented in Table 6), is regarded as the response. These values are subjected to numerical analysis using Qblade to validate their accuracy. This analysis aims to assess the disparity between the outcomes derived from mathematical optimization methods and those obtained from the Qblade analytical method. The design parameters specified in Table 6 underwent a redesign and reanalysis using Qblade to compare and validate them against the analytical optimization results. Additionally, Fig. 14 displays C_p values resulting from various optimization methods, contrasting them with the base control case that was not subjected to any optimization method.

The data presented in Fig. 14 illustrates a significant enhancement in rotor efficiency. This improvement was attained through the optimization of conceptual design parameters, reanalyzed using QBlade rather than optimization analytical applications, in comparison to the results observed in the base control case. The data indicates that the optimal configuration offers a wider operational range compared to the base control case. Notably, the factorial method, which suggested the largest rotor diameter, outperformed other methods when reanalyzed with Qblade. Specifically, the maximum C_p values achieved with Qblade, based on the optimal design parameters obtained by the factorial, RSM, and Kriging methods, showed an increase of 11%, 5%, and 5.6%, respectively, compared to the base control case. In Table 7, it is evident that Qblade produced a higher maximum C_p when utilizing design parameters from the factorial method during reanalysis compared to C_p values obtained through other optimization approaches. However, when comparing the C_p results obtained from the reanalysis of the turbine based on the optimized geometry by Qblade with the C_p values generated through optimization via analytical programs based on mathematical relations, a significant discrepancy in the maximum C_p values was observed. This comparison indicates that the factorial method with a 7.7% difference with Qblade results may be less reliable in predicting outcomes than other optimization methods. The percentage difference observed between the analytical results derived from Qblade and those obtained through mathematical analysis programs can be accurately calculated by comparing the results. It is important to note that the higher error percentage associated with the factorial method is typical, as this approach utilizes fewer layers for optimization. Consequently, while this method is readily accessible and offers rapid computation, it reduces accuracy. Consequently, the RSM and Kriging techniques, which incorporate a more elaborate solution matrix and utilize additional layers for optimization, have demonstrated higher accuracy in their result. While this marginal difference does not discredit the optimization method, it does emphasize the need to compare results obtained from analytical applications with those from Qblade, which employs BEM coupling with actual disk theory for result analysis. Generally, an optimization method demonstrating the lowest error percentage compared to numerical simulations with Qblade is considered more valid. In Fig. 15, the optimized rotor is juxtaposed with a small-scale rotor derived from the experimental modeling conducted by Akour et al [39]. This comparison aims to enhance the understanding of the rotor's optimal performance.

According to Fig. 15, Akour et al [39]. experimental results are consistent with the recent numerical outcomes derived from the analytical solution provided by the Qblade package. The agreement between the current numerical results and previous experimental simulations can emphasize the solid validity of this simulation. Additionally, it has been established that the optimized geometry proposed in this study demonstrates superior performance compared to the small-scale rotor designed with the SG6043 airfoil profile, particularly in its operational ability at a wider TSR range.

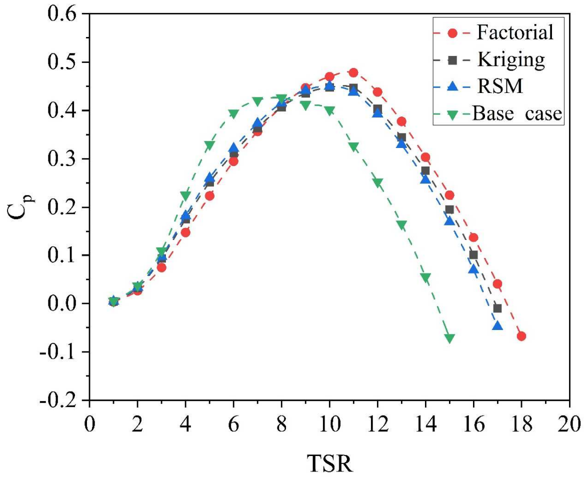

Fig. 14. C_p values for different optimization methods compared to the base case.

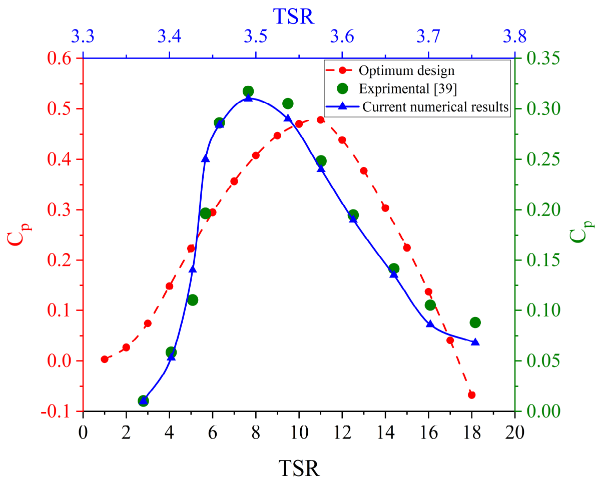

Fig. 15. Comparison of experimental and numerical results for the small HAWT alongside the optimized rotor.

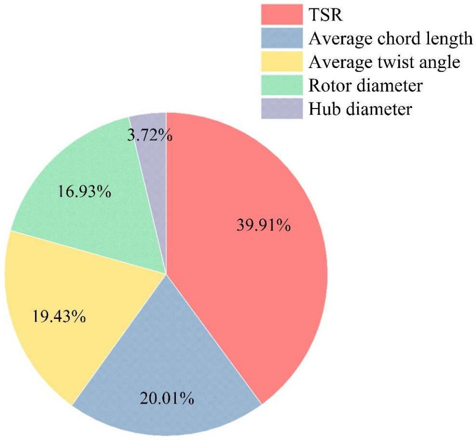

Fig. 16. Sensitivity analysis.

The results of the sensitivity analysis of turbine C_p with respect to individual design parameters and TSR are given in Fig. 16. Upon thoroughly examining Fig. 16, it has become apparent that the TSR of the HAWT had the greatest impact on its efficiency accounting for 39.91% of the variability. This underscores the critical role of the operating range in optimizing outcomes. Additionally, we found that among the various design parameters, the chord length distribution had the greatest influence, accounting for 20.01% of the variability in rotor efficiency. Conversely, the hub diameter had the least impact, at 3.72%. The sensitivity analysis has facilitated the conceptual design of HAWT by identifying which design parameters significantly influence turbine efficiency. Consequently, it is imperative to allocate greater precision to these parameters. TSR, which is highly dependent on wind velocity and operating conditions, has been identified as a critical factor. Additionally, it is noteworthy that variations in blade radius also impact efficiency, alongside wind velocity and rotational speed, which are related to TSR mathematical relation. Beyond TSR, changes in the average chord length exhibit considerable design relevance.

6. Conclusion

In this study, a parametric evaluation was carried out on a small HAWT. Subsequently, three different optimization methods were applied to identify the optimum configuration, with a focus on determining the most effective optimization method. It is crucial to optimize conceptual design parameters with TSR as an input to determine the optimal C_p. This method offers a comprehensive view for designing HAWT under optimal conditions and enhances understanding of the rotor's operational range based on TSR. The results obtained from the parametric study with Qblade commercial package and optimization with three different methods namely Kriging, factorial, and RSM, revealed that:

- The study on the rotor diameter revealed that the turbine with a large diameter has a broader operational range and generates higher available power. While smaller rotors face performance challenges at large TSRs, they exhibit better self-start capability. In addition, the numerical results showed that a smaller hub diameter is more optimal and marginally enhances HAWT performance.
- The study of the number of HAWT rotor blades demonstrated that three-bladed turbines have a wider operating range, while the 7-bladed turbines, characterized by high solidity, face fewer challenges in initiating rotation.
- Distributions for twist angle and chord length along the radial positions were considered, with the average value as the input parameter. Results indicated that the case with the highest twist angle yields the lowest efficiency and operational range. Meanwhile, the case with the shortest chord length gives the highest C_p values and output power.
- S-series and NACA series profiles, both symmetric and asymmetric, were evaluated. Following an assessment of their aerodynamic performance, including the lift and drag forces at different AOAs, it was found that the SG6043 profile from S-series airfoils and the NACA4412 asymmetric airfoil from the NACA series airfoils provided the most favorable conditions.
- Between three optimization methods, RSM method has the lowest error percentage; making it a potentially more reliable choice compared to other methods. Nevertheless, all optimization methods yielded an increase in the maximum C_p compared to the initial base geometry.
- The simulation results for the optimized rotor were compared to a small-scale HAWT, and the proposed rotor demonstrated significantly better performance. Also, the previous experimental and current numerical results emphasized the validity of the simulation.
- Sensitivity analysis results indicated that the average chord length distribution had the most significant impact on the current HAWT performance.

7. Future Studies

For future investigations, it is recommended that the parametric study be subject to CFD modeling. This approach would enable the examination of the impact of each design parameter on turbine efficiency, as well as the analysis of the flow physics around the blades and the aerodynamic performance. By employing CFD modeling, we can obtain a more thorough understanding of the impact of the design parameters on both the turbine's efficiency and the flow characteristics like wake flow.

Author Contributions

F. Ghafoorian planned the scheme, initiated the project, and suggested the simulations, conducted the simulations and analyzed the results; H. Wan supervised the project, developed the mathematical modeling, reviewed the results and analyzed the results; S. Chegini generated figures. The manuscript was written through the contribution of all authors. All authors discussed the results, reviewed, and approved the final version of the manuscript.

Acknowledgments

Not applicable.

Conflict of Interest

The authors declared no potential conflicts of interest concerning the research, authorship, and publication of this article.

Funding

The authors received no financial support for the research, authorship, and publication of this article.

Data Availability Statements

The datasets generated and/or analyzed during the current study are available from the corresponding author on reasonable request.

Nomenclature

Symbols		Subscript	
L	Lift force (N)	t	Tangential
D	Drag force (N)	n	Normal
B	Number of blades	h	Hub
V	Wind velocity (m/s)	**Greek**	
P	Output power (W)	ρ	Density (kg/m^3)
R	Rotor radius (m)	α	Angle of attack
A	Axial induction factors	φ	Inflow angle
a'	Radial induction factors	σ	Solidity
A	Airfoil Area (m^2)	β	Twist angle (Degree)
C_p	Power coefficient	θ_p	Pitch angle (Degree)
C_L	Lift coefficient	ω	Angular velocity (rad/s)
C_D	Drag coefficient	λ_r	Local tip speed ration
c	Chord length (m)		
Abbreviations			
HAWT	Horizontal Axis Wind Turbine		
BEM	Blade Element Momentum		
DOE	Design of Experiments		
AOA	Angle of Attack		
RSM	Response Surface Method		
TSR	Tip Speed Ratio		

References

[1] Sayed, E.T., Olabi, A.G., Alami, A.H., Radwan, A., Mdallal, A., Rezk, A., Abdelkareem, M.A., Renewable energy and energy storage systems, *Energies*, 16(3), 2023, 1415.
[2] Letcher, T., *Wind energy engineering: a handbook for onshore and offshore wind turbines*, Elsevier, 2023.
[3] Dixon, S.L., Hall, C.A., *Fluid mechanics and thermodynamics of turbomachinery*, Seventh edition, Butterworth-Heinemann, Amsterdam, 2014.
[4] ArabGolarcheh, A., Anbarsooz, M., Benini, E., An actuator line method for performance prediction of HAWTs at urban flow conditions: A case study of rooftop wind turbines, *Energy*, 292, 2024, 130268.
[5] Roy, S., Das, B., Biswas, A., A comprehensive review of the application of bio-inspired tubercles on the horizontal axis wind turbine blade, *International Journal of Environmental Science and Technology*, 20(4), 2023, 4695–4722.
[6] Zhang, Z., Liu, X., Zhao, D., Post, S., Chen, J., Overview of the development and application of wind energy in New Zealand, *Energy and Built Environment*, 4(6), 2023, 725–742.
[7] Sithole, T.S., Veeredhi, V.R., Sithebe, T., Implementation and Evaluation of a Low Speed and Self-Regulating Small Wind Turbine for Urban Areas in South Africa, *Engineering Technology and Applied Science Research*, 13(2), 2023, 10553–10558.
[8] Guo, W., Gong, S., Shen, Z., Gong, Y., Lu, H., Effects of internal rotor parameters on the performance of curved blade-straight blade vertical axis wind turbine, *Energy Conversion and Management*, 321, 2024, 119078.
[9] Mauro, S., Lanzafame, R., Messina, M., Brusca, S., On the importance of the root-to-hub adapter effects on HAWT performance: A CFD-BEM numerical investigation, *Energy*, 275, 2023, 127456.
[10] Shen, Z., Gong, S., Xie, G., Lu, H., Guo, W., Investigation of the effect of critical structural parameters on the aerodynamic performance of the double Darrieus vertical axis wind turbine, *Energy*, 290, 2024, 130156.
[11] Koc, E., Gunel, O., Yavuz, T., Comparison of Qblade and CFD results for small-scaled horizontal axis wind turbine analysis, *IEEE International Conference on Renewable Energy Research and Applications*, Birmingham, United Kingdom, IEEE, 2016, 204–209.
[12] Sedighi, H., Akbarzadeh, P., Salavatipour, A., Aerodynamic performance enhancement of horizontal axis wind turbines by dimples on blades: Numerical investigation, *Energy*, 195, 2020, 117056.
[13] Ohiemi, I.E., Sunsheng, Y., Singh, P., Li, Y., Osman, F., Evaluation of energy loss in a low-head axial flow turbine under different blade numbers using entropy production method, *Energy*, 274, 2023, 127262.
[14] Alaskari, M., Abdullah, O., Majeed, M.H., Analysis of Wind Turbine Using QBlade Software, *IOP Conference Series: Materials Science and Engineering*, 518(3), 2019, 032020.
[15] Kriswanto et al., Power Optimization of The Horizontal Axis Wind Turbine Capacity of 1 MW on Various Parameters of The Airfoil, an Angle of Attack, and a Pitch Angle, *Journal of Advanced Research in Fluid Mechanics and Thermal Sciences*, 103(2), 2023, 141–156.
[16] Mujahid, M., Rafai, A., Imran, M., Saggu, M.H., Rahman, N., Design Optimization and Analysis of Rotor Blade for Horizontal-Axis Wind Turbine Using Q-Blade Software, *Pakistan Journal of Scientific and Industrial Research Series A: Physical Sciences*, 64(1), 2021, 65–75.
[17] Muhsen, H., Al-Kouz, W., Khan, W., Small Wind Turbine Blade Design and Optimization, *Symmetry*, 12(1), 2019, 18.
[18] Oukassou, K., Mouhsine, S.E., Hajjaji, A.E., Kharbouch, B., Comparison of the power, lift and drag coefficients of wind turbine blade from aerodynamics characteristics of Naca0012 and Naca2412, *Procedia Manufacturing*, 32, 2019, 983–990.

[19] Hasan, M.E., Eltayesh, A., Awaad, M.I., El-Batsh, H.M., Experimental Examination for the Electric Power Generation of a Commercial Small-scale Wind Turbine with Modified Aerodynamic Design, *Alexandria Engineering Journal*, 64, 2023, 25–39.
[20] Shen, Z., Gong, S., Lu, H., Guo, W., Chen, W., Investigation of the effect of pitch angle of double Darrieus vertical axis wind turbine based on aerodynamic performance and entropy production theory, *Ocean Engineering*, 311, 2024, 118930.
[21] Suresh, A., Rajakumar, S., Design of small horizontal axis wind turbine for low wind speed rural applications, *Materials Today: Proceedings*, 23, 2020, 16–22.
[22] Kunya, B.I., Folayan, C.O., Pam, G.Y., Anafi, F.O., Muhammad, N.M., Performance study of Whale-Inspired Wind Turbine Blade at Low Wind Speed Using Numerical Method, *CFD Letters*, 11(7), 2019, 11–25.
[23] Zhang, Z., Dong, R., Tan, D., Zhang, B., Multi-objective optimization of performance characteristic of diesel particulate filter for a diesel engine by RSM-MOPSO during soot loading, *Process Safety and Environmental Protection*, 177, 2023, 530–545.
[24] Qian, J., et al., Multi-objective optimization design of the wind-to-heat system blades based on the Particle Swarm Optimization algorithm, *Applied Energy*, 355, 2024, 122186.
[25] Zuo, W., Li, D., Li, Q., Cheng, Q., Zhou, K., E, J., Multi-objective optimization of multi-channel cold plate under intermittent pulsating flow by RSM and NSGA-II for thermal management of electric vehicle lithium-ion battery pack, *Energy*, 283, 2023, 129085.
[26] Akhlagi, M., Ghafoorian, F., Mehrpooya, M., Sharifi Rizi, M., Effective Parameters Optimization of a Small Scale Gorlov Wind Turbine, Using CFD Method, *Iranian Journal of Chemistry and Chemical Engineering*, 42(7), 2023, 2286-2304.
[27] Shen, Z., Gong, S., Zu, H., Guo, W., Multi-objective optimization study on the performance of double Darrieus hybrid vertical axis wind turbine based on DOE-RSM and MOPSO-MODM, *Energy*, 299, 2024, 131406.
[28] Veza, I., Spraggon, M., Fattah, I.M.R., Idris, M., Response surface methodology for optimizing engine performance and emissions fueled with biofuel: Review of RSM for sustainability energy transition, *Results in Engineering*, 18, 2023, 101213.
[29] Marten, D., Wendler, J., *QBlade Guidelines v0.6*, 2013.
[30] Manwell, J.F., McGowan, J.G., Rogers, A.L., *Wind energy explained: theory, design and application*, John Wiley & Sons, 2010.
[31] Mohammadi, H., *Kriging-based black-box global optimization: analysis and new algorithms*, Diss. Ecole Nationale Supérieure des Mines de Saint-Etienne, 2016.
[32] Uy, M., Telford, J.K., Optimization by Design of Experiment techniques, *IEEE Aerospace Conference*, 2009, 1–10.
[33] Han, Z.-H., Zhang, K.-S., Surrogate-based optimization, *Real-world Applications of Genetic Algorithms*, 343, 2012, 343–362.
[34] Youn, P., Dong, B., *Surrogate Modeling or Response Surface Methodology*, Mechanical and Aerospace Engineering, Seoul National University, Korea, 2017.
[35] Cardoso Netto, D., Ramirez Camacho, R., Manzanares Filho, N., Surrogate-Based Design Optimization of a H-Darrieus Wind Turbine Comparing Classical Response Surface, Artificial Neural Networks, and Kriging, *Journal of Applied Fluid Mechanics*, 16(4), 2023, 703-716.
[36] Chegini, S., Ghafoorian, F., Moghimi, M., Mehrpooya, M., Optimized arrangement of clustered Savonius VAWTs, Techno-Economic evaluation and feasibility of installation, *Iranian Journal of Chemistry and Chemical Engineering*, 43(2), 2024, 875-894.
[37] Vieceli, N., et al., Solvent extraction of cobalt from spent lithium-ion batteries: Dynamic optimization of the number of extraction stages using factorial design of experiments and response surface methodology, *Separation and Purification Technology*, 307, 2023, 122793.
[38] Sobieczky, H., *Parametric airfoils and wings*, Recent development of aerodynamic design methodologies: inverse design and optimization, 1999, 71–87.
[39] Akour, S.N., Al-Heymari, M., Ahmed, T., Khalil, K.A., Experimental and theoretical investigation of micro wind turbine for low wind speed regions, *Renewable Energy*, 116, 2018, 215–223.

ORCID iD

Farzad Ghafoorian https://orcid.org/0009-0005-4714-8699
Hui Wan https://orcid.org/0000-0001-6227-710X
Sahel Chegini https://orcid.org/0009-0004-3509-274X

© 2024 Shahid Chamran University of Ahvaz, Ahvaz, Iran. This article is an open access article distributed under the terms and conditions of the Creative Commons Attribution-NonCommercial 4.0 International (CC BY-NC 4.0 license) (http://creativecommons.org/licenses/by-nc/4.0/).

How to cite this article: Ghafoorian F., Wan H., Chegini S. A Systematic Analysis of a Small-Scale HAWT Configuration and Aerodynamic Performance Optimization Through Kriging, Factorial, and RSM Methods, *J. Appl. Comput. Mech.*, 11(4), 2025, 887-903. https://doi.org/10.22055/jacm.2024.47896.4822

Publisher's Note Shahid Chamran University of Ahvaz remains neutral with regard to jurisdictional claims in published maps and institutional affiliations.